https://doi.org/10.1038/s44384-026-00068-3

The flexural SSH-type model: Topology and edge states in elastic beam systems

Giorgio Carta[1], Ioannis Ioannou Sougleridis[2,3,4], Lorenzo Morini[1] & Michele Brun[1] ✉

We study the topological properties of slender flexural waveguides subject to kinematic constraints that selectively suppress rotations or transverse displacements. By deriving the 2 × 2 Bloch Hamiltonian, which possesses sublattice symmetry, we map the continuous flexural system onto the discrete Su-Schrieffer-Heeger (SSH) model and characterize its band topology. The emergence of topological edge states is also predicted by the quantized values of the Zak phase. In addition, we examine finite configurations with different boundary conditions to demonstrate bulk-boundary correspondence, revealing edge modes localized at either end depending on the termination and the coupling parameters. We further introduce elastic boundary springs as tunable elements to continuously control the existence and localization of edge modes. The present framework lays the groundwork for future extensions to more general flexural models, incorporating all kinematic variables, more elaborate boundary conditions, and additional physical effects.

In recent years, topological insulators have inspired the design of a new class of wave-based systems across a wide range of physical domains, including photonics[1–3], mechanics[4,5], and acoustics[6–8]. A defining feature of topological systems is the emergence of robust, spatially localized states at their boundaries or interfaces, which are protected against disorder and imperfections. Owing to their fundamental importance, topologically-protected edge wave phenomena have been studied in quantum systems[9,10], acoustics[11], photonics[12,13], and mechanics[14–25].

In this context, the one-dimensional Su-Schrieffer-Heeger (SSH) chain[26,27] is a canonical model, with non-trivial topology and established bulk-boundary correspondence[28]. In essence, in the bulk of the system, a topological invariant can be defined, directly related to the underlying symmetries of the system[29]. The values of the topological invariant depend on the parameters of the Hamiltonian of the model and take integer values, which correspond to the number of localized and robust bound states in a finite system with vanishing boundary conditions[28,30].

Beyond its original formulation, the SSH model has been extended in numerous directions, encompassing both one- and higher-dimensional realizations[31–45]. Within this broader framework, an increasing number of studies have demonstrated that acoustic and one-dimensional mechanical systems can be accurately captured using SSH-type descriptions[46–52]. In parallel, the field of acoustic and mechanical metamaterials has undergone rapid development[53], with increasing attention devoted to their topological properties and to experimental realizations spanning two-[21,37,54–56] and even three-[57,58] dimensional architectures. In particular, some studies have examined mechanically isostatic systems with topological properties, either based on the SSH model[59] or involving three-dimensional structures[60].

However, a rigorous connection between a structural/mechanical waveguide and the SSH model is still lacking. To the best of our knowledge, no direct mapping between structural/mechanical waveguides and the SSH model–as well as other models in the context of topological insulators–has been established without relying on lumped-element descriptions, fitting models, or tight-binding approximations. Here, we introduce a continuous flexural waveguide, and propose a mapping to the SSH model within the framework of the Euler-Bernoulli beam theory. In practice, we provide a simple and general framework for investigating the topological phases of continuous beam structures, while highlighting in depth the importance of boundary conditions in establishing bulk-boundary correspondence and obtaining accurate predictions of the edge states.

In this work, as a prototype of flexural waveguide, we introduce a two-phase structured Euler-Bernoulli beam with pinned or, alternatively, sliding supports at the junctions between the distinct phases. By exploiting the physical constraints associated with the considered supports, we switch from a fourth-order to a second-order formulation of the flexural wave propagation problem. For periodic infinite systems, we analytically derive a discrete SSH model corresponding to the second-order reduced continuous flexural problem. We show how the dispersion relation of the continuous structured beam can be obtained from the non-trivial solutions of the

[1]Department of Mechanical, Chemical and Materials Engineering, University of Cagliari, Cagliari, Italy. [2]Laboratoire d'Acoustique de l'Université du Mans (LAUM), Institut d'Acoustique—Graduate School (IA-GS), CNRS, Le Mans Université, Le Mans, France. [3]Department of Physics, National and Kapodistrian University of Athens, University Campus, Athens, Greece. [4]PMMH, ESPCI Paris, Université PSL, CNRS, Sorbonne Université, Université Paris Cité, Paris, France.
✉e-mail: michele.brun@unica.it

eigenvalue problem associated with the discrete SSH equivalent model. The chiral symmetry (also known as bipartite or sublattice symmetry[29]) of the associated SSH model allows for the definition of a topological invariant, in this case the winding number[30], while the mirror symmetry implies the quantization of the Zak phase[28]. We discuss how the sublattice and mirror symmetries guarantee the equivalence between the winding number and the Zak phase[27] in determining the existence of boundary states in cases of appropriate interface and boundary conditions[46,61–63]. Beyond the linear regime considered here, the interplay of nonlinearity and non-trivial topology has recently been investigated in[64], showing the importance of chiral/sublattice and particle-hole symmetries.

The general setup developed for periodic infinite waveguides is then adapted to study finite-sized systems considering both Neumann and Dirichlet boundary conditions. For both pinned and sliding supports, we show the existence of edge modes and discuss the effects of the boundary conditions and the symmetries of the considered structured beams on their properties. In addition, we demonstrate that interface modes can occur at the same frequencies as the edge modes in structures made of two insulators with distinct topological properties. Finally, a parametric analysis is carried out to study the transition of edge modes obtained with different termination constraints by introducing Robin-type boundary conditions, which are implemented via elastic supports in the form of rotational or translational springs.

Results

Bi-phase flexural pin-supported waveguides

Firstly, we study the topological properties of flexural waveguides consisting of bi-phase Euler-Bernoulli beams with pinned supports at the junctions between different phases. We start by introducing periodic infinite systems and examining their analogy with the well-known SSH model[26,27]. Subsequently, we analyze both symmetric and non-symmetric finite-sized structures, discussing the influence of different boundary conditions on the existence of edge and interface modes.

The periodic structure consists of an infinite repetition of two distinct phases of Euler-Bernoulli beams, with pinned (or hinged) supports at the junctions between phases A and B (see Fig. 1a). The length, Young's modulus, mass density, cross-sectional area and second moment of area of each phase i (where i = A, B) are denoted as l_i, E_i, ρ_i, A_i and I_i, respectively. The total length of each elementary cell is designated as L.

In this work, we study only flexural waves, described by the small amplitude transverse displacement $v(x, t)$, where x is the axial coordinate and t is time. In particular, we assume time-harmonic conditions, whereby $v(x, t) = V(x)\mathrm{e}^{-\mathrm{i}\omega t}$, with ω being the radian frequency and $V(x)$ representing the transverse displacement amplitude. Henceforth, all kinematic and static variables will be expressed in terms of their amplitudes, and the term "amplitude" will be omitted for brevity.

For a structure composed of beam elements, such as the one depicted in Fig. 1a, the generalized vector of kinematic and static variables typically includes four components, namely the transverse displacement $V(x)$, the rotation $\Theta(x)$, the bending moment $M(x)$ and the shear force $T(x)$, resulting in a 4×4 transfer matrix[65]. However, since at the pinned supports the displacements are fixed to zero, the generalized vector of the beam element is reduced to two components[66]: its rotation $\Theta(x) = V'(x)$ (the kinematic field) and its bending moment $M(x) = -EI\Theta'(x) = -EIV''(x)$ (the dual static field). Consequently, the 4×4 transfer matrix is simplified to a 2×2 transfer matrix. The expression for the latter is given by (16).

Following the mapping procedure described in the Methods section, we retrieve the eigenvalue problem

$$\begin{pmatrix} 0 & u + w\,\mathrm{e}^{-\mathrm{i}kL} \\ u + w\,\mathrm{e}^{\mathrm{i}kL} & 0 \end{pmatrix} \begin{pmatrix} \mathcal{A} \\ \mathcal{B} \end{pmatrix} = E(\beta l) \begin{pmatrix} \mathcal{A} \\ \mathcal{B} \end{pmatrix}, \tag{1}$$

where

$$E(\beta l) = \frac{\cos(\beta l) - \coth(\beta l)\,\sin(\beta l)}{1 - \operatorname{csch}(\beta l)\,\sin(\beta l)}, \quad u = \frac{Q_A}{Q_A + Q_B}, \; w = \frac{Q_B}{Q_A + Q_B}, \tag{2}$$

with

$$Q_i = \sqrt[4]{\rho_i A_i \left(E_i I_i\right)^3}\ (i = \text{A or B}). \tag{3}$$

In the equations above, k is the wavenumber and βl is the frequency parameter (see (11)). We note that the eigenvalue $E(\beta l)$ corresponds to either of the identical diagonal terms of the transfer matrix in (16). In addition to using the rotation as the mapping variable, an equivalent mapping can be established by employing the bending moment, following an approach similar to that in[47,50]. We refer the reader to the Methods section for details.

The coupling coefficients u and w, defined in (2), are real and positive quantities that meet the condition $u + w = 1$. Consequently, the matrix in (1) has the same structure as the Bloch Hamiltonian of the SSH model. The spectral parameter $E(\beta l)$ of the bulk problem, interpreted as the energy eigenvalue in the quantum SSH model, is a function of the frequency parameter βl, and it is broadband, as long as the Euler-Bernoulli approximation is valid[67]. The broadband validity of the mapping is different from the majority of elastic and mechanical topological systems, which resort to lumped-element[47,54] or fitting models, which thus have limited tunability.

The dispersion relation is determined from the non-trivial solutions of the eigenvalue problem (1), resulting in

$$E(\beta l) = \pm\sqrt{u^2 + w^2 + 2uw\cos(kL)}. \tag{4}$$

Due to the sublattice symmetry, the spectrum $E(\beta l)$ is symmetric with respect to $E(\beta l) = 0$, which occurs for $\beta l \simeq (n + 1/4)\pi \quad (n \in \mathbb{N}^+)$. In Fig. 2, we show the dispersion curves for three different values of the coupling pair (u, w): specifically, $u = 0.25$, $w = 0.75$ (inset (a)); $u = w = 0.5$ (inset (b)); and $u = 0.75$, $w = 0.25$ (inset (c)). Since the periodic waveguide is continuous, it supports infinite dispersion bands. In panel (b), corresponding to $u = w = 0.5$ (i.e., when phases A and B are dynamically identical), a band closing occurs, whereas in panel (c) a band inversion is observed with respect to panel (a). All dispersion curves exhibit a zero-frequency band gap, as well as band gaps at higher frequencies, due to the pinned supports. These band

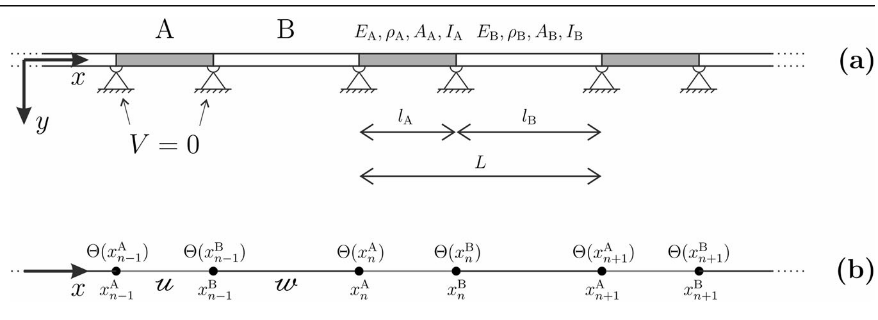

Fig. 1 | Mapping of the periodic flexural beam system to an SSH-type lattice. a Periodic system of elastic beams composed of two phases (denoted as A and B), supported by pins at the junctions between the phases. **b** Mapping to the discrete SSH model.

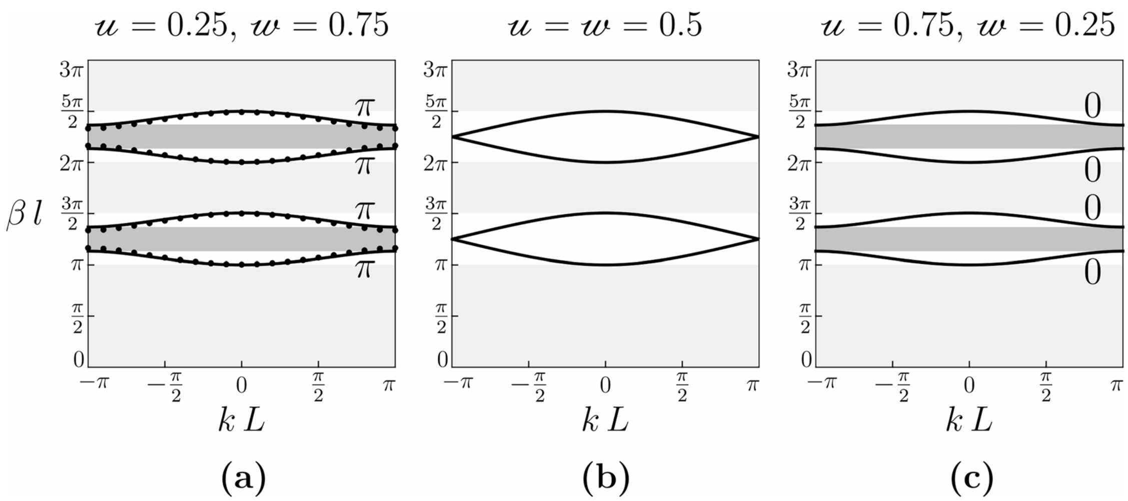

Fig. 2 | Dispersion curves and Zak phase of the periodic flexural system with pinned supports. Dispersion curves for the system shown in Fig. 1, for different values of the coupling terms: **a** $u = 0.25$, $w = 0.75$; **b** $u = w = 0.5$; **c** $u = 0.75$, $w = 0.25$. Band gaps are highlighted in gray. The values of the Zak phase $\vartheta_n^{\mathrm{Zak}}$ associated with the displayed bands are also indicated. The dots in panel (**a**) are obtained from three-dimensional finite element simulations, where the beams are modeled as solids.

gaps are denoted by light shaded regions, while the band gaps associated with the periodicity of the waveguide when $u \neq w$ are highlighted by dark shaded regions.

The Euler-Bernoulli beam model provides an accurate approximation for thin solids whose cross-sectional dimensions are significantly smaller than their length. In Fig. 2a, the dispersion curves obtained from alternative finite element computations are indicated by dots. In these simulations, still based on modal analysis incorporating quasi-periodicity conditions, the elements are modeled as thin solids rather than beams; in particular, we have taken $E_{\mathrm{A}} = E_{\mathrm{B}} = 210$ GPa, $\rho_{\mathrm{A}} = \rho_{\mathrm{B}} = 7800\ \mathrm{kg/m^3}$ (steel beams), $l_{\mathrm{A}} = 1$ m, $l_{\mathrm{B}} = 1.1699$ m, and square cross-sections of side length equal to 1 cm (phase A) and 1.3687 m (phase B), yielding $\beta_{\mathrm{A}} l_{\mathrm{A}} = \beta_{\mathrm{B}} l_{\mathrm{B}} = \beta l$. The results show good agreement with the analytical predictions based on the Euler-Bernoulli beam theory.

We can observe that the Hamiltonian (1) has sublattice symmetry, allowing for the definition of a topological invariant, which, in the case of the SSH model, is the *winding number*[27]. We also note that, in addition to sublattice symmetry, the system possesses mirror symmetry, since $\boldsymbol{PT} = \boldsymbol{T}^{-1}\boldsymbol{P}$, with $\boldsymbol{P} = \mathrm{diag}[-1, 1]$. The mirror symmetry implies that the values of the *Zak phase*[68], defined below in this section, can take only two integer values, 0 or π, that correspond to two phases, trivial or topological, respectively. We note that in this framework the Zak phase is mod(2π). The presence of both the sublattice and mirror symmetry provides an algebraic connection between the quantized values of the Zak phase and the winding number (see, for example,[27]). By ensuring that bulk-boundary correspondence is satisfied[28,69,70] (see also next section), the Zak phase can be used as a bulk quantity to probe the emergence of edge modes in finite lattices, for appropriate boundary terminations or interfaces[46,47,71], where translational symmetry is broken.

The Zak phase associated with the n-th band is defined as[72]

$$\vartheta_n^{\mathrm{Zak}} = -\mathrm{Im}\int_{-\pi/\mathrm{L}}^{\pi/\mathrm{L}} \langle \boldsymbol{\Phi}, \partial_{\mathrm{k}}\boldsymbol{\Phi}\rangle \mathrm{dk}, \tag{5}$$

where $\langle\rangle$ represents the Hermitian inner product, $\boldsymbol{\Phi}$ is the normalized eigenvector evaluated at the wavenumber k for the n-th band, and $\partial_k\boldsymbol{\Phi}$ is its derivative with respect to k. Although it is not strictly necessary to compute the Zak phase for the SSH model[27], for completeness we compute it numerically as follows:

$$\vartheta_n^{\mathrm{Zak}} \simeq -\mathrm{Im}\sum_{i=1}^{N_k-1} \boldsymbol{\Phi}_i^{\dagger}\left(\boldsymbol{\Phi}_{i+1} - \boldsymbol{\Phi}_i\right) \simeq -\mathrm{Im}\sum_{i=1}^{N_k-1} \log\left(\boldsymbol{\Phi}_i^{\dagger}\boldsymbol{\Phi}_{i+1}\right), \tag{6}$$

where † denotes the conjugate transpose and N_k is the number of values of k considered in the numerical calculations. Due to the mirror symmetry, the values obtained by expression (5) or alternatively (6) are quantized to either 0 or π. According to the sublattice symmetry of the Hamiltonian (1), $\vartheta_n^{\mathrm{Zak}}$ is related to the winding number ν_n of the n-th band through the expression $\vartheta_n^{\mathrm{Zak}} = \pi\nu_n$. Consequently, $\vartheta_n^{\mathrm{Zak}} = \pi$ corresponds to $\nu_n = 1$ and to one topologically protected edge mode, which can be observed in a corresponding finite-sized structure with appropriate boundary conditions. Conversely, for $\vartheta_n^{\mathrm{Zak}} = 0$ we have $\nu_n = 0$, and no topologically protected edge modes can be detected in an associated finite waveguide. The value of the Zak phase is appended to every dispersion curve in Fig. 2. We point out that, since $\vartheta_n^{\mathrm{Zak}} = \pi$, topologically protected edge modes are expected for finite waveguides characterized by $u < 0.5$ or, equivalently, $w > 0.5$.

Finite pin-supported structures and bulk-boundary correspondence

In this section, we examine beam systems composed of a finite number of repetitive cells, set to 20 in our calculations, and determine their eigenfrequencies (eigenvalues) and eigenmodes (eigenvectors). The latter are the eigensolutions in terms of transverse displacements evaluated at the corresponding eigenfrequencies. We impose different boundary conditions to investigate how they affect the eigenspectra of the systems.

In the numerical computations, we assume that the two phases are steel beams of square cross-section with identical constitutive properties, namely $E_{\mathrm{A}} = E_{\mathrm{B}} = 210$ GPa and $\rho_{\mathrm{A}} = \rho_{\mathrm{B}} = 7800\ \mathrm{kg/m^3}$. Regarding the geometrical parameters, for phase A we set the length equal to $l_{\mathrm{A}} = 1$ m and the side length of the square-cross section equal to $s_{\mathrm{A}} = 1$ cm; conversely, the geometrical properties of phase B are determined such that the coupling term u (or w) takes the specified value and that $\beta_{\mathrm{A}} l_{\mathrm{A}} = \beta_{\mathrm{B}} l_{\mathrm{B}} = \beta l$, namely $s_{\mathrm{B}} = ((1-u)/u)^{2/7}\, s_{\mathrm{A}}$ and $l_{\mathrm{B}} = \sqrt{s_{\mathrm{B}}/s_{\mathrm{A}}}\, l_{\mathrm{A}}$. Nonetheless, we point out that the above values for the material and geometrical parameters are only indicative, since the results depend on the non-dimensional quantities u (or w) and βl.

We start from the finite structure shown in Fig. 3a, which presents a hinged support—vanishing displacement and bending moment—at the left end and a clamped support—vanishing displacement and rotation—at the right end. At the interfaces between phases A and B, pinned supports are applied, as in Fig. 1. In the 2×2 restriction induced by the supports, the hinged and clamped supports on the boundaries identify, respectively, Neumann and Dirichlet boundary conditions. As shown in[47,50], different boundary conditions require different mapping variables in order to ensure bulk-boundary correspondence[28,70]. In the present system, a hinged

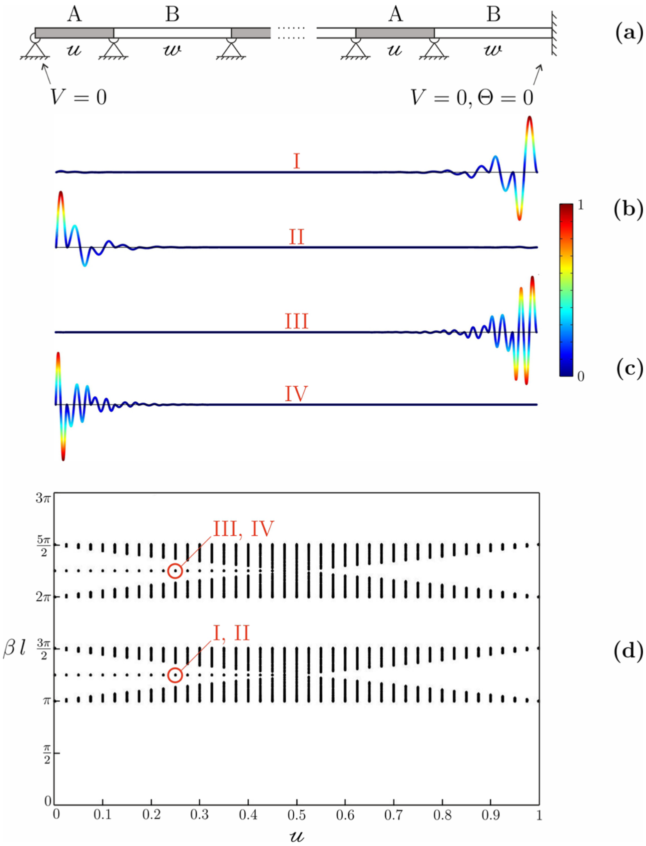

Fig. 3 | Edge modes and eigenspectrum in a finite flexural system with pinned supports and distinct boundary conditions. a Finite structure featuring a hinge–vanishing displacement and bending moment–at the left end and a clamp–vanishing displacement and rotation -- at the right end. **b**, **c** Edge modes detected in the first and second band gaps, which are localized on either boundary of the finite structure, respectively, of the corresponding periodic system for u = 0.25. In this and all subsequent figures, the eigenmodes are normalized so that their maximum value is equal to 1. **d** Eigenfrequencies for different values of the coupling term u.

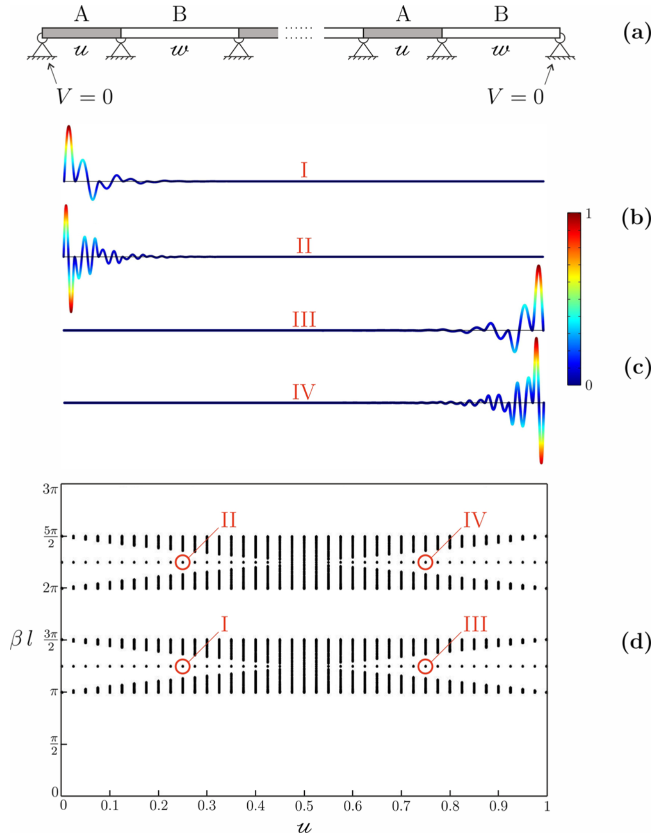

Fig. 4 | Edge modes and eigenspectrum in a finite flexural system with hinged boundary conditions. a Finite system of beams with hinged supports at both boundaries. **b**, **c** Edge modes observed for u = 0.25 and u = 0.75, respectively. **d** Eigenspectrum versus coupling term u.

boundary condition enforces a vanishing bending moment, making it the appropriate variable for predicting topological edge modes. Conversely, for a clamped boundary condition, the rotation vanishes and therefore constitutes the correct mapping variable. For a finite lattice with mixed boundary conditions (hinged on the left and clamped on the right), each end of the structure can be effectively isolated, and treated as a semi-infinite chain, provided that the number of unit cells is sufficiently large. Consequently, the influence of each boundary condition and its connection to the bulk can be analyzed independently. Finally, we note that for brevity we shall only use the couplings u and w of the rotation mapping in the following analysis, while keeping in mind that for the bending moment mapping the couplings are inversed (refer to the "Methods" section).

The first two clusters of eigenvalues are reported in Fig. 3d for different values of u (here we remind that the system admits an infinite number of eigenfrequencies, since it is continuous). As expected, the eigenfrequencies associated with spatially extended eigenmodes, which have support throughout the entire system, lie within the pass bands of the corresponding periodic system. Moreover, additional eigenstates localized at the edges of the structure appear for u < 0.5, occurring for $E(\beta l)$=0 and, hence, $\beta l \simeq (n + 1/4)\pi \quad (n \in \mathbb{N}^+)$. For each of these values of βl, two coincident eigenfrequencies are obtained, associated with two edge modes, one localized at the right end and the other at the left end (see Fig. 3b, c for $\beta l \simeq 5\pi/4$ and $\beta l \simeq 9\pi/4$, respectively). We also note that, if the constraints at the two boundaries are swapped, the same results are retrieved, but for u > 0.5 (the corresponding results are not shown here for brevity).

In Fig. 4 we consider the same structure as in Fig. 3, but with hinges at both ends. Here, the applicable mapping variable is the bending moment. Also in this case, edge modes are found for $\beta l \simeq (n + 1/4)\pi \quad (n \in \mathbb{N}^+)$; however, with the constraints as in Fig. 4a, edge modes emerge for all values of the coupling u. In particular, when u < 0.5 (u > 0.5) the edge states are localized at the left (right) end. On the other hand, when the two ends are clamped, the opposite behavior is observed, i.e., an edge mode is detected on the right (left) boundary when u < 0.5 (u > 0.5).

As a third example, we consider the system shown in Fig. 5a, which has clamped ends (implying that the corresponding mapping variable is the rotation), and phases arranged as "BA …BAB". All eigenvalues are included in Fig. 5d as functions of u. As in the case examined in Fig. 3, edge modes occur only for u < 0.5, and each dot represents a pair of coincident eigenfrequencies. Nonetheless, in the present configuration, localization appears at both ends, with symmetric and antisymmetric mode shapes (see Fig. 5b, c). Referring to the same structure with the pattern "BA …BAB", but when the two ends are hinged, we observe the same behavior, but for u > 0.5. Conversely, when the left end is clamped and the right end is hinged, the same conclusions drawn for the case in Fig. 4 also apply here. Localization occurs at the opposite edge when the boundary constraints are swapped.

We remark that the observations in the previous paragraph are reversed when the phases follow the pattern "AB …ABA". Namely, the results are the same as those obtained for the structure "BA …BAB" under the substitution $u \to (1 - u)$.

Finally, we present an example of a localised mode at the interface between two insulators. To the left of the interface, we consider the finite structure with the pattern "AB …AB" and hinged supports. To its right, we connect the same structure, but mirrored, so that phases A and B are exchanged (see Fig. 6a). As expected, a localised mode is observed at the

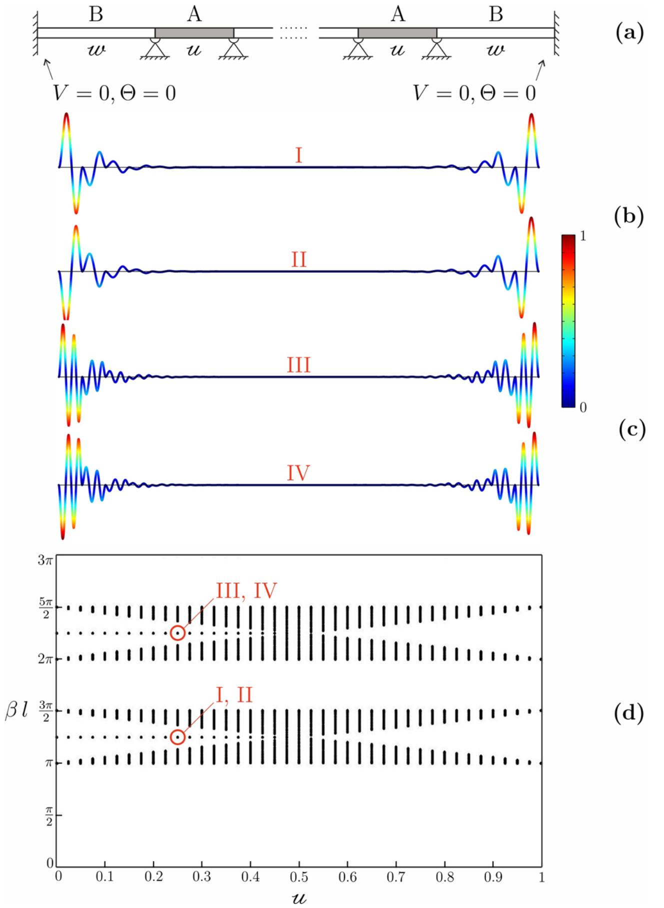

Fig. 5 | Edge modes and eigenspectrum in a finite flexural system with clamped boundary conditions. **a** Finite system of beams with clamped supports at both ends, that starts and ends with phase B. **b**, **c** Edge modes observed for $u = 0.25$ within the first and second stop-band, respectively. **d** Eigenspectrum for various coupling strengths u.

interface, at the same frequency as the edge modes. Two such interfacial modes, occurring for $\beta l \simeq 5\pi/4$ and $\beta l \simeq 9\pi/4$, are illustrated in Fig. 6b.

Modulated Robin-type boundary conditions for the pin-supported structures

The systems illustrated in Figs. 4a, 3a share the same internal structure and the same boundary condition at the left end, but differ in the constraint applied at the right end, namely a hinge in the former and a clamp in the latter. Both configurations can be represented by the system shown in Fig. 7a, which presents a hinge equipped with a rotational spring of stiffness $K_{\rm R}$ at the right end. In particular, setting $K_{\rm R} = 0$ (or $K_{\rm R} \to \infty$) recovers the structure with the hinge in Fig. 4a (or the configuration with the clamp in Fig. 3a). Accordingly, the rotational spring can be used as a modulation parameter, enabling a continuous transition between the two structures in Figs. 4a, 3a. We note that the rotational stiffness at the boundary is a Robin-type boundary condition, and breaks the bulk-boundary correspondence for both the rotation and bending moment mappings. However, as we approach the limits $K_{\rm R} \to 0$ and $K_{\rm R} \to \infty$, we asymptotically recover the bulk-boundary correspondence.

In Fig. 7b, the eigenfrequencies obtained across several values of the coupling term u and five distinct values of the normalized rotational stiffness $\widetilde{K}_{\rm R}$ are reported, where $\widetilde{K}_{\rm R} = K_{\rm R} l_{\rm A}/(E_{\rm A} I_{\rm A})$. From the diagrams, it is apparent that if $\widetilde{K}_{\rm R}$ is small (e.g., $\widetilde{K}_{\rm R} = 0.05$), the eigenspectrum of Fig. 4d is recovered, with the eigenfrequencies corresponding to the localized edge modes becoming higher for larger values of u. Consequently, the edge modes localized on the right boundary do not occur at

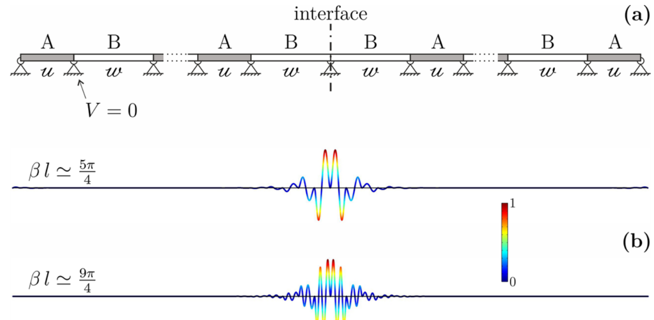

Fig. 6 | Interface modes at the boundary between flexural systems with distinct topological phases. **a** Structure comprising two insulators connected at an interface. **b** Localised modes observed at the interface, obtained for $\beta l \simeq 5\pi/4$ and $\beta l \simeq 9\pi/4$.

$E(\beta l) = 0$, as required by the sublattice symmetry in the SSH model, due to the presence of the Robin-type boundary condition which does not satisfy bulk-boundary correspondence. In addition, as the normalized rotational stiffness increases, the localized modes observed for $u > 0.5$ progressively disappear, as in the case $\widetilde{K}_{\rm R} = 5$. For sufficiently large $\widetilde{K}_{\rm R}$, additional frequencies associated with edge modes emerge for $u < 0.5$. In the limit $\widetilde{K}_{\rm R} \to \infty$, the eigenspectrum of Fig. 3d (exhibiting for $u < 0.5$ two coincident eigenfrequencies, corresponding to two localized modes at the opposite ends) is retrieved, as expected. Overall, the results in Fig. 7 illustrate the gradual transition between the structures in Figs. 4a, 3a as the rotational stiffness is varied.

To further illustrate the transition described above, Fig. 8a, c show the eigenfrequencies computed for fixed values of the coupling term ($u = 0.75$ and $u = 0.25$, respectively) while varying the normalized rotational stiffness $\widetilde{K}_{\rm R}$. From Fig. 8a, it is possible to roughly identify the value of $\widetilde{K}_{\rm R}$ for which the edge mode disappears within each stop-band. A precise threshold cannot be determined, as the localisation of the mode progressively weakens. This behavior is demonstrated in Fig. 8b, where two edge modes depicted in the first and second band gaps and exhibiting weak localisation are included. In the range $u \in (0, 0.5)$ (e.g., $u = 0.25$ as in Fig. 8c), for sufficiently large values of the normalized rotational stiffness, an additional edge mode appears in each stop-band at a frequency that increases with $\widetilde{K}_{\rm R}$. In the limit when $\widetilde{K}_{\rm R} \to \infty$, corresponding to a clamped end, the eigenfrequencies coincide, as also shown in Fig. 3d. Figure 8d illustrates two eigenmodes localized at the opposite ends, corresponding to two closely spaced eigenfrequencies.

Bi-phase flexural structure with sliding supports

Now, we study systems of Euler-Bernoulli beams with sliding supports that allow transverse displacements but prevent rotations. We first investigate the topological properties of a periodic infinite bi-phase flexural waveguide and subsequently examine the existence of edge modes in finite structures with different boundary conditions.

We refer to the periodic system shown in Fig. 9a, consisting of an infinite repetition of phases A and B, supported by sliders at the junctions. Since rotations are restricted at these locations, the only kinematic variable is the transverse displacement V, while the dual static variable is the shear force T. As demonstrated for the waveguide with pinned supports, the 4×4 transfer matrix is simplified to a 2×2 transfer matrix, which is given by (27).

Upon completing the necessary algebraic operations, we obtain the eigenvalue problem:

$$\begin{pmatrix} 0 & \overline{u} + \overline{w}\,\mathrm{e}^{-\mathrm{i}kL} \\ \overline{u} + \overline{w}\,\mathrm{e}^{\mathrm{i}kL} & 0 \end{pmatrix} \begin{pmatrix} \mathcal{C} \\ \mathcal{D} \end{pmatrix} = \overline{E}(\beta l) \begin{pmatrix} \mathcal{C} \\ \mathcal{D} \end{pmatrix}, \tag{7}$$

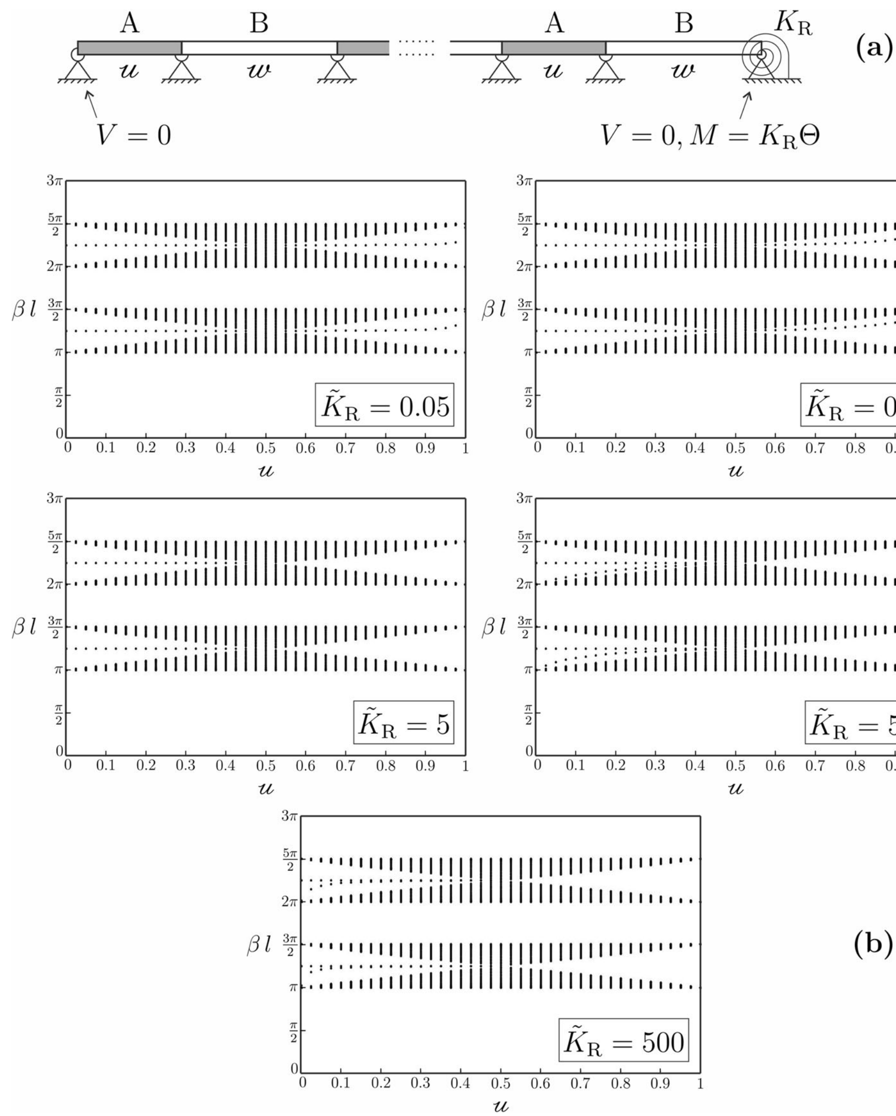

Fig. 7 | Control of the eigenspectrum via a rotational spring at a boundary. a Finite structure with a hinge—Neumann boundary condition—on the left end and a hinge with a rotational spring—Robin-type boundary condition—on the right end, where K_R denotes the rotational spring stiffness. **b** Eigenspectra of the finite structure in (**a**), evaluated over a range of coupling terms u and five values of the normalized rotational spring stiffness $\tilde{K}_R$.

where

$$\overline{E}(\beta l) = \frac{\cos(\beta l)+\coth(\beta l)\,\sin(\beta l)}{1+\operatorname{csch}(\beta l)\,\sin(\beta l)}, \qquad \overline{u} = \frac{P_A}{P_A+P_B}, \ \overline{w} = \frac{P_B}{P_A+P_B}, \ \overline{u}+\overline{w} = 1, \tag{8}$$

with

$$P_i = \sqrt[4]{\left(\rho_i A_i\right)^3 E_i I_i} \ (i = \mathrm{A\ or\ B}). \tag{9}$$

We point out that $\overline{E}(\beta l)$ is equal to either of the diagonal terms of the transfer matrix in Eq. (27), and $\overline{E}(\beta l) = 0$ for $\beta l \simeq (n - 1/4)\pi \quad (n \in \mathbb{N}^+)$. As for the flexural waveguide with pinned supports, in addition to the displacement mapping, an equivalent mapping can be established by employing the shear force as the mapping variable[47,50], as detailed in the Methods section.

The dispersion curves, determined by $\overline{E}(\beta l) = \pm\sqrt{\overline{u}^2 + \overline{w}^2 + 2\overline{u}\,\overline{w}\cos(kL)}$, are shown in Fig. 10 for $\overline{u} = 0.25$, $\overline{w} = 0.75$ (inset (a)); $\overline{u} = \overline{w} = 0.5$ (inset (b)); $\overline{u} = 0.75$, $\overline{w} = 0.25$ (inset (c)). Differently from the structure with pinned supports, no zero-frequency band gap appears in this case, as transverse displacements are allowed. Band inversion is observed for $\overline{u} = \overline{w} = 0.5$. In addition, the values of the Zak phase for the dispersion bands included in the diagram are reported in the same figure. We note that the lowest band is not differentiable at $kL = 0$; however, considering that the band is symmetric with respect to positive and negative values of kL and that it is differentiable in the domain $kL \in (0, \pi]$, we calculated the Zak phase over this interval and doubled the result to obtain the value for $-\pi \le kL \le \pi$. Comparing Figs. 10 and 2, we note similarities in the behavior of the systems with pinned and sliding supports, which suggests similar features in the existence and properties of edge modes, as shown in the following.

Finite structures with sliding supports

We study finite structures consisting of 20 unit cells and endowed with different constraints at the ends, in order to investigate the effect of the boundary conditions on the emergence of edge modes. In the 2 × 2 restriction, the sliding and clamped supports on the boundaries identify Neumann and Dirichlet boundary conditions, respectively.

Similarly to the case of pinned supports, the numerical simulations are carried out by considering the two phases as steel beams with square cross-sections and identical material properties, namely $E_A = E_B = 210$ GPa and $\rho_A = \rho_B = 7800\,\mathrm{kg/m^3}$. With reference to the geometrical parameters, phase A is assigned a length $l_A = 1$ m and a square-cross section with side length $s_A = 1$ cm; on the other hand, the geometrical properties of phase B are chosen so that the coupling term $\overline{u}$ (or $\overline{w}$) assumes the prescribed value and $\beta_A l_A = \beta_B l_B = \beta l$, in particular $s_B = ((1-\overline{w})/\overline{w})^{2/5} s_A$ and $l_B = \sqrt{s_B/s_A}\, l_A$. It should be emphasized again that the above material and geometrical parameters are reported only for

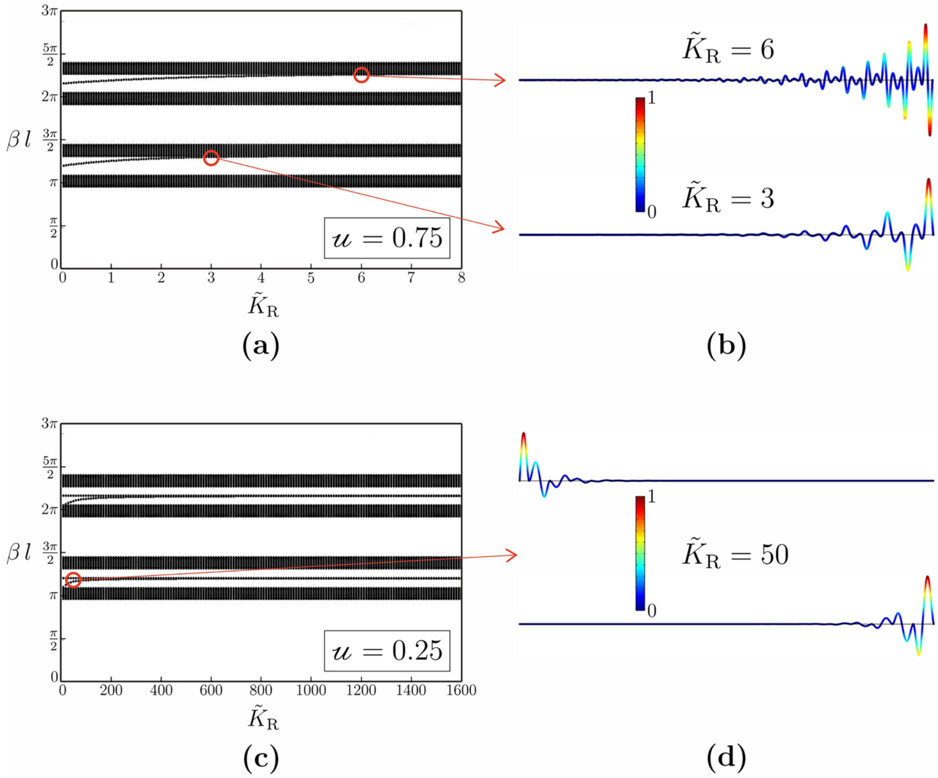

Fig. 8 | Emergence and evolution of edge modes with increasing rotational spring stiffness. **a** Eigenspectrum calculated for several values of $\widetilde{K}_{\mathrm{R}}$ and $u = 0.75$. **b** Examples of edge modes exhibiting weak localization. **c** Eigenfrequencies versus $\widetilde{K}_{\mathrm{R}}$ for $u = 0.25$. **d** Eigenmodes for $\widetilde{K}_{\mathrm{R}} = 50$, associated with two closely spaced eigenfrequencies.

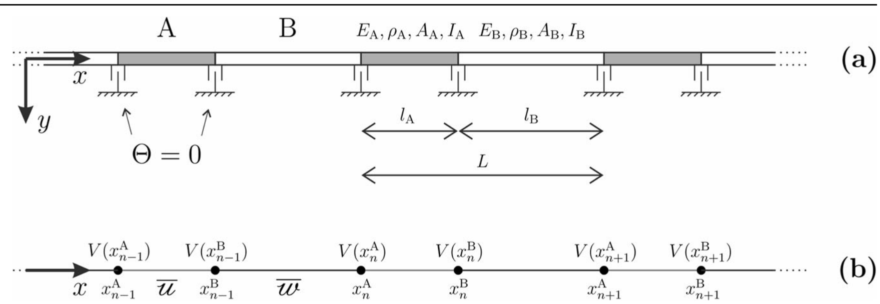

Fig. 9 | Mapping of the periodic flexural system with sliding supports to an SSH-type lattice. **a** Periodic system of elastic beams made of two phases (A and B), having sliding supports at the junctions. **b** Mapping to the discrete SSH model.

completeness, since the results ultimately depend on the non-dimensional quantities $\overline{u}$ (or $\overline{w}$) and βl.

As discussed for the system with pinned supports, in the context of bulk-boundary correspondence[28,70], different boundary conditions require different mapping variables. In the present system, a sliding boundary condition enforces a vanishing shear force, making it the appropriate variable for predicting topological edge modes. Conversely, for a clamped boundary condition, the displacement vanishes and therefore constitutes the correct mapping variable. For a finite lattice with mixed boundary conditions (slider on the left and clamp on the right), each end of the structure can be effectively isolated and treated as a semi-infinite chain, provided that the number of unit cells is sufficiently large. Consequently, the influence of each boundary condition and its connection to the bulk can be analyzed independently. Finally, for brevity, we shall only use the couplings $\overline{u}$ and $\overline{w}$ of the displacement-based mapping in the following analysis, while keeping in mind that for the shear force-based mapping the couplings are inversed, as shown in the Methods section.

We begin by considering the system represented in Fig. 11a, characterized by an "AB …AB" pattern and featuring a slider on the left end (preventing only rotations) and a clamp on the right end (constraining both rotations and transverse displacements). The eigenspectrum for different values of the coupling term $\overline{u}$ is reported in Fig. 11b. As in Fig. 3, we notice that edge modes appear only for $\overline{u} < 0.5$; however, in the present case they occur for $\beta l \simeq (n - 1/4)\pi \quad (n \in \mathbb{N}^+)$. For each of these values of βl, two coincident eigenfrequencies are found, associated with two edge modes localized at the right and left ends, as shown in the insets of Fig. 11b.

In the structure depicted in Fig. 12, the clamp at the right end is replaced by a slider, while preserving the "AB …AB" pattern of Fig. 11. This modification of the boundary condition at the right end leads to the appearance of edge modes over the entire range $\overline{u} \in (0, 1)$. Nonetheless, in contrast to the case of Fig. 11, each point at $\beta l \simeq (n - 1/4)\pi \quad (n \in \mathbb{N}^+)$ corresponds to a single eigenfrequency. This configuration is analogous to the scenario examined in Fig. 4, where rotations at the junctions were allowed.

The transition between the scenarios described in Figs. 12, 11 can be achieved by introducing a translational spring of stiffness K_{T} at the right end (Robin-type boundary condition), as illustrated in Fig. 13a. The spring stiffness is increased to establish a continuous variation between the structure in Fig. 12 and that in Fig. 11. To this end, we introduce the normalized translational stiffness $\widetilde{K}_{\mathrm{T}} = K_{\mathrm{T}} l_{\mathrm{A}}^3/(E_{\mathrm{A}} I_{\mathrm{A}})$.

In Fig. 13b, we set the coupling parameter $\overline{u} = 0.75$ and calculate the eigenfrequencies for several values of $\widetilde{K}_{\mathrm{T}}$. As $\widetilde{K}_{\mathrm{T}}$ is increased, we observe that the eigenfrequencies associated with edge modes migrate and eventually merge into the bulk bands of the system. For $\overline{u} = 0.75$, and more generally

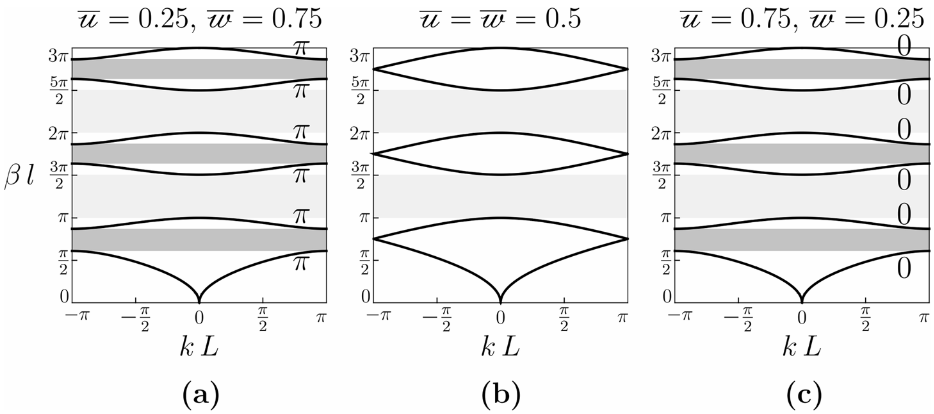

Fig. 10 | Dispersion curves and Zak phase of the periodic flexural system with sliding supports. Dispersion curves for the system shown in Fig. 9, for different values of the coupling terms: **a** $\overline{u} = 0.25$, $\overline{w} = 0.75$; **b** $\overline{u} = \overline{w} = 0.5$; **c** $\overline{u} = 0.75$, $\overline{w} = 0.25$. Band gaps are highlighted in gray. The values of the Zak phase associated with the displayed bands are also indicated.

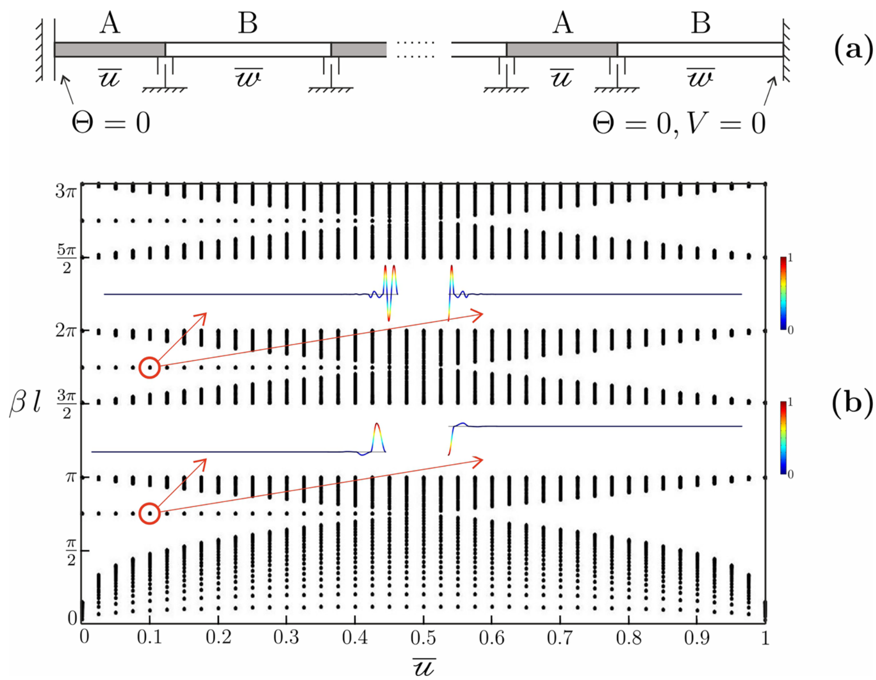

Fig. 11 | Edge modes and eigenspectrum in a finite flexural system with sliding supports and distinct boundary conditions. a Finite structure with a slider (Neumann boundary condition) and a clamp (Dirichlet boundary condition) at the left and right end, respectively. **b** Eigenfrequencies for several values of the coupling term $\overline{u}$ and examples of edge modes, calculated for $\overline{u} = 0.1$.

for $\overline{w} > 0.5$, edge modes tend to disappear; the corresponding critical values of $\widetilde{K}_{\mathrm{T}}$ depend on the band under consideration and are difficult to identify precisely due to the gradual nature of the transition. Examples of weakly localized edge modes are shown in Fig. 13c.

In Fig. 13d, the coupling term is taken as $\overline{u} = 0.25$. In this case, and more generally for $\overline{u} < 0.5$, each odd stop-band induced by the structural heterogeneity contains a constant eigenfrequency branch corresponding to an edge mode. In addition, a second branch of edge-mode eigenfrequencies emerges at finite values of $\widetilde{K}_{\mathrm{T}}$, until the two branches coalescence in the limit $\widetilde{K}_{\mathrm{T}} \to \infty$ (representing a clamped end). In Fig. 13e we present two localized edge modes with closely spaced frequencies.

Discussion

The occurrence of edge modes in a continuous flexural waveguide system with periodically constrained kinematic components has been investigated by mapping the governing equations onto the classical SSH model. This analogy shows that edge modes arise under Neumann boundary conditions in phase A and under Dirichlet boundary conditions in phase B when the parameter $u < 1/2$. Analogous results are obtained for $u > 1/2$, when the boundary constraints associated with the two phases are exchanged. When the free kinematic variable at the junctions between different phases is the rotation (displacement), Neumann boundary conditions correspond to hinged (sliding) constraints, whereas Dirichlet boundary conditions correspond to clamped ends.

Consistent with previous studies in solid-state physics and acoustics, as long as bulk-boundary correspondence is satisfied—which is achieved by choosing the appropriate mapping variable for the corresponding boundary condition—the eigenfrequencies of the localized edge modes in the finite structure coincide with the zeros of the bulk Hamiltonian energy.

In particular, for simplicity, we refer to Fig. 3, where the mode localized at the left boundary exhibits non-zero rotations only at the A-type nodes[27]. Specifically, $\Theta(x_1^{\mathrm{A}}) \neq 0$ denotes the rotation at the boundary node, whereas $\Theta(x_i^{\mathrm{B}}) = 0$ for $i = 1, 2, \ldots$. On the other hand, the topological nature of the mode localized at the right boundary can be justified by exploiting the dual formulation presented in the "Methods" section. In this dual representation, where the mapped variable is the bending moment M, the right edge mode remains topologically protected, since it localizes on the sublattice of A-type nodes where the moments are non-zero, while $M(x_i^{\mathrm{B}}) = 0$ for $i = \ldots, N-1, N$.

To clarify this point, we refer to Fig. 14. Panel (a) shows the rotations in the vicinity of the left boundary for the left end topologically protected mode at $\beta l \simeq 5\pi/4$, where $E(\beta l) = 0$. As expected, the rotations are non-zero only at the A-type nodes. For the right end protected mode, panel (b) shows that the rotations vanish at the A-type nodes (with node A_N located at the

Fig. 12 | Edge modes and eigenspectrum in a finite flexural system with sliding boundary conditions. **a** Finite system with sliders at both ends. **b** Eigenspectrum versus $\overline{u}$ and instances of edge modes, evaluated for $\overline{u} = 0.1$ and $\overline{u} = 0.9$.

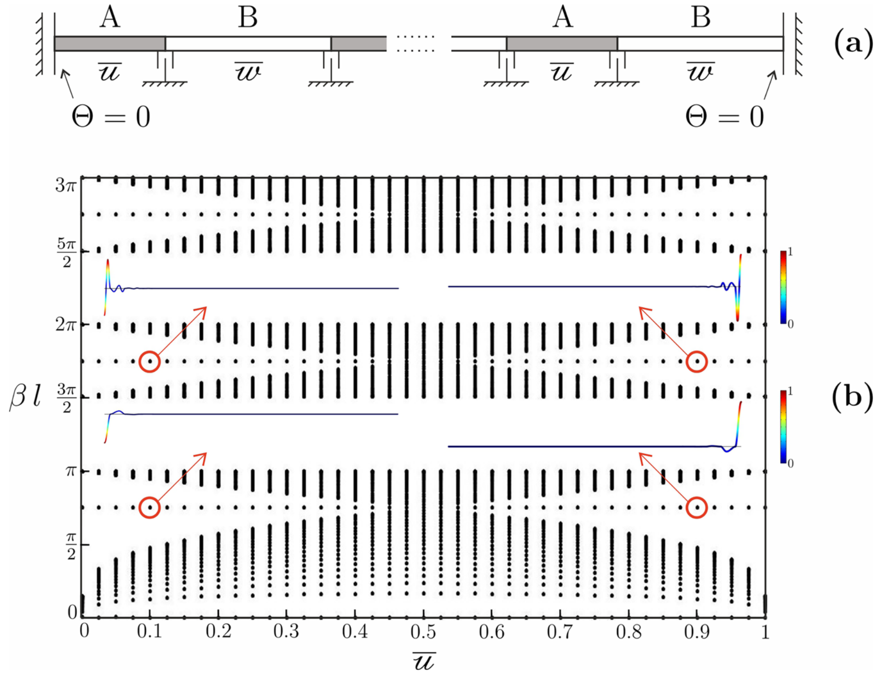

Fig. 13 | Control of the eigenspectrum via a translational spring at a boundary. **a** Finite structure with a slider at the left end and a slider equipped with a translational spring of stiffness K_T at the right end. **b** Eigenfrequencies for different values of the normalized translational stiffness $\widetilde{K}_T$ (on a $\log_{10}$-scale), calculated for $\overline{u} = 0.75$. **c** Eigenmodes computed for $\overline{u} = 0.75$ and for specific values of $\widetilde{K}_T$, as detailed in the figure. **d**, **e** Same as in (**b**, **c**), but for $\overline{u} = 0.25$.

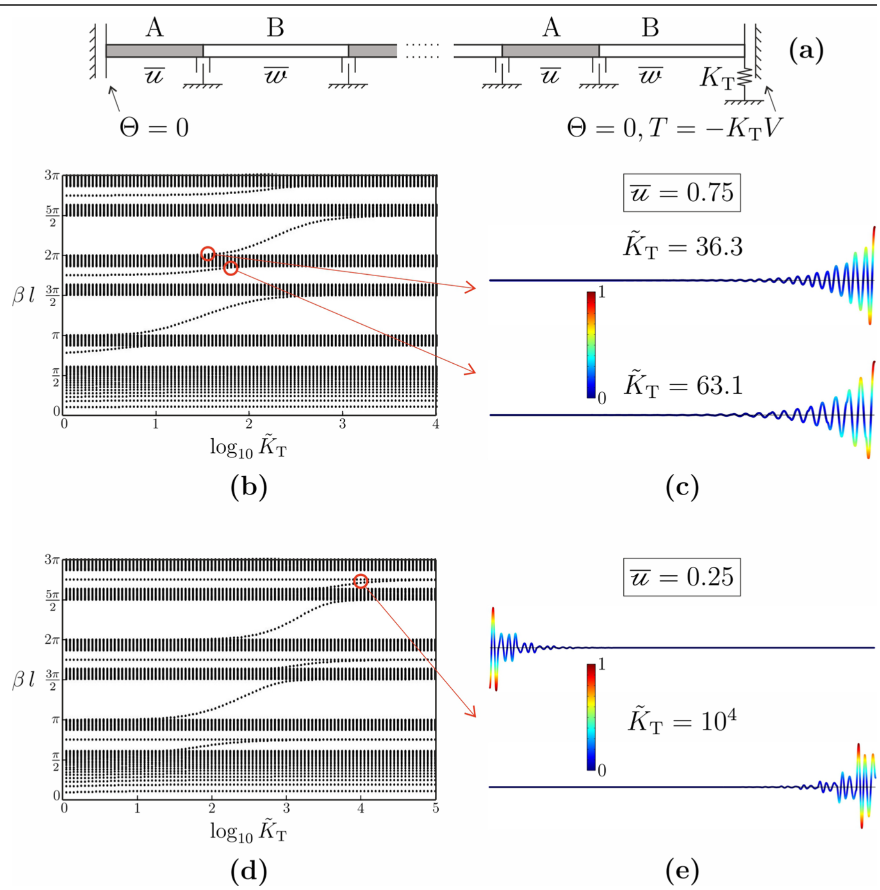

boundary), which may suggest a trivial mode. However, the dual formulation in terms of nodal bending moments shares the same eigenfrequency but yields different eigenvectors[47,50]. In this representation, the sublattice supporting non-zero bending moments is again the set of A-type nodes. This result confirms the robustness of the edge mode localized at the right end.

In this work, we have proposed a general framework to investigate the existence and topology of edge and interface modes in mechanical systems modeled as microstructured media. Future developments will extend the present formulation to more general configurations in which all kinematic variables at the junctions are admissible, leading to a 4×4 bulk Hamiltonian. Moreover, the proposed results are broadband and

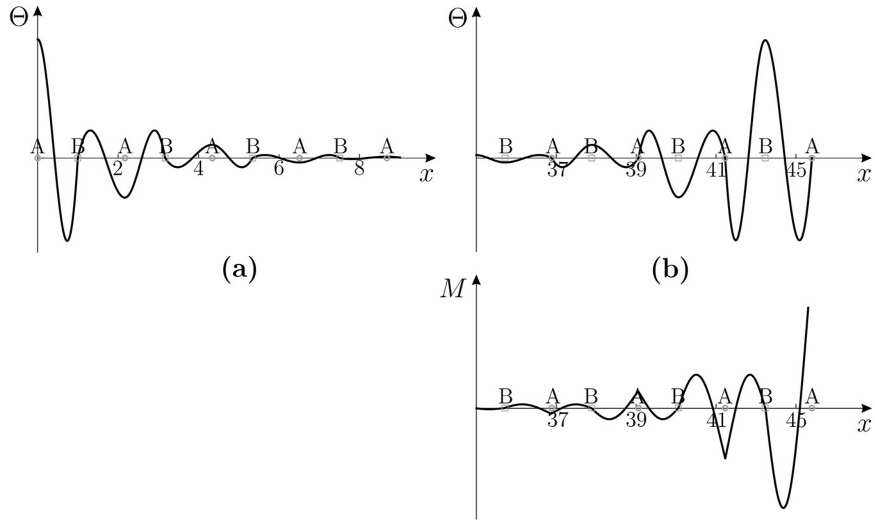

Fig. 14 | Kinematic (rotation) and static (bending moment) field distributions of topological edge modes in the finite flexural pin-supported system. **a** Rotation field in the structure of Fig. 3a, evaluated for $\varkappa = 0.25$ and $\beta l \simeq 5\pi/4$, associated with the edge mode localized at the left end. **b** Rotation (above) and bending moment (below) fields in the structure of Fig. 3a, evaluated for $\varkappa = 0.25$ and $\beta l \simeq 5\pi/4$, corresponding to the edge mode localized at the right end.

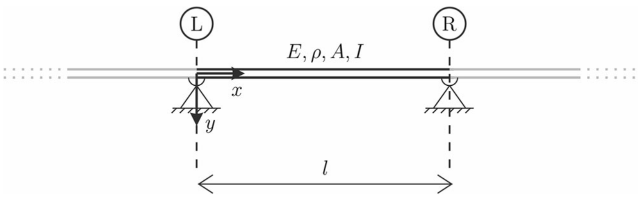

Fig. 15 | Reference configuration of a flexural beam with pinned supports. Elastic beam with pinned supports at the left (L) and right (R) ends, having length l, Young's modulus E, mass density ρ, area A and second moment of area I.

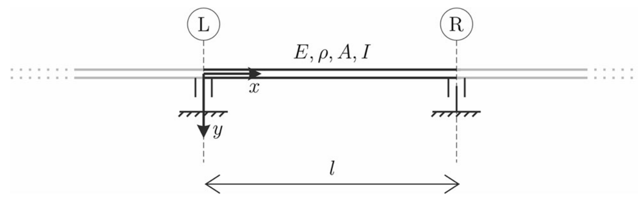

Fig. 16 | Reference configuration of a flexural beam with sliding supports. Elastic beam with sliding supports at the left (L) and right (R) ends, with length l, Young's modulus E, mass density ρ, area A and second moment of area I.

remain accurate within the validity range of the Euler-Bernoulli approximation, as confirmed by independent 3D finite element simulations. More refined beam theories are expected to further extend the frequency range over which agreement with the continuous structural models can be achieved.

Methods

Derivation of the transfer matrix for an Euler-Bernoulli beam element with pinned supports

Consider an Euler-Bernoulli beam of length l, Young's modulus E, mass density ρ, area A and second moment of area I. Its flexural motion in the time-harmonic regime is described by the transverse displacement amplitude $V(x)$, where x is the axial coordinate (refer to Fig. 15). At its left and right boundaries, the transverse displacement is restrained by pinned supports.

The expression of the transverse displacement amplitude at a generic position x is given by[73]

$$V(x) = A_1 \cos(\beta x) + A_2 \sin(\beta x) + A_3 \cosh(\beta x) + A_4 \sinh(\beta x), \quad (10)$$

where $A_1, \ldots, A_4$ are unknown coefficients and

$$\beta = \sqrt[4]{\frac{\rho A \omega^2}{EI}}, \quad (11)$$

with ω denoting the radian frequency.

By imposing the boundary conditions $V(x = 0) = 0$ and $V(x = l) = 0$, we determine the constants A_3 and A_4 in terms of A_1 and A_2. Introducing a change of variables from A_1 and A_2 to B_1 and B_2, defined by $B_1 = -\beta A_1$ and $B_2 = \beta A_2$, we obtain the expressions for the rotation amplitude $\Theta(x) = V'(x)$ and the bending moment amplitude $M(x) = -EI\Theta'(x)$, that can be written in matrix form as follows:

$$\boldsymbol{\Psi}(x) = \begin{pmatrix} \Theta(x) \\ M(x) \end{pmatrix} = \boldsymbol{S}(x)\boldsymbol{B}, \quad (12)$$

where $\boldsymbol{\Psi}(x)$ is the generalized vector containing the kinematic and static variables for this case, $\boldsymbol{B} = \left(B_1 B_2\right)^{\mathrm{T}}$ is the vector of unknowns, and

$$\boldsymbol{S}(x) = \begin{pmatrix} \begin{array}{c} \sin(\beta x) + \sinh(\beta x) \\ +\mathcal{F}(\beta l)\cosh(\beta x) \end{array} & \cos(\beta x) - \mathcal{G}(\beta l)\cosh(\beta x) \\ \begin{array}{c} -EI\beta\left[\cos(\beta x) + \cosh(\beta x) \right. \\ \left. +\mathcal{F}(\beta l)\sinh(\beta x)\right] \end{array} & EI\beta[\sin(\beta x) + \mathcal{G}(\beta l)\sinh(\beta x)] \end{pmatrix}, \quad (13)$$

with

$$\begin{aligned} \mathcal{F}(\beta l) &= \tfrac{\cos(\beta l) - \cosh(\beta l)}{\sinh(\beta l)}, \\ \mathcal{G}(\beta l) &= \tfrac{\sin(\beta l)}{\sinh(\beta l)}. \end{aligned} \quad (14)$$

Evaluating the generalized vector at the left ($x_{\mathrm{L}} = 0$) and right ($x_{\mathrm{R}} = l$) ends, we obtain respectively:

$$\begin{aligned} \boldsymbol{\Psi}(x_{\mathrm{L}}) &= \boldsymbol{S}(x_{\mathrm{L}})\boldsymbol{B}, \\ \boldsymbol{\Psi}(x_{\mathrm{R}}) &= \boldsymbol{S}(x_{\mathrm{R}})\boldsymbol{B} = \boldsymbol{S}(x_{\mathrm{R}})\boldsymbol{S}^{-1}(x_{\mathrm{L}})\boldsymbol{\Psi}(x_{\mathrm{L}}) = \boldsymbol{T}\boldsymbol{\Psi}(x_{\mathrm{L}}). \end{aligned} \quad (15)$$

In the latter formula, we have denoted by $\boldsymbol{T} = \boldsymbol{S}(x_{\mathrm{R}})\boldsymbol{S}^{-1}(x_{\mathrm{L}})$ the *transfer matrix* for a beam element with pinned supports at the ends, which results in

$$\boldsymbol{T} = \begin{pmatrix} \frac{\cos(\beta l) - \coth(\beta l)\,\sin(\beta l)}{1 - \operatorname{csch}(\beta l)\,\sin(\beta l)} & \frac{\cos(\beta l)\coth(\beta l) - \operatorname{csch}(\beta l)}{-EI\beta\left[1 - \operatorname{csch}(\beta l)\,\sin(\beta l)\right]} \\ \frac{2EI\beta\,\sin(\beta l)}{1 - \operatorname{csch}(\beta l)\,\sin(\beta l)} & \frac{\cos(\beta l) - \coth(\beta l)\,\sin(\beta l)}{1 - \operatorname{csch}(\beta l)\,\sin(\beta l)} \end{pmatrix}. \quad (16)$$

We note that $\det(\boldsymbol{T}) = 1$, and

$$\boldsymbol{T}^{-1} = \begin{pmatrix} \frac{\cos(\beta l) - \coth(\beta l)\sin(\beta l)}{1 - \operatorname{csch}(\beta l)\sin(\beta l)} & \frac{\cos(\beta l)\coth(\beta l) - \operatorname{csch}(\beta l)}{EI\beta[1 - \operatorname{csch}(\beta l)\sin(\beta l)]} \\ \frac{-2EI\beta\sin(\beta l)}{1 - \operatorname{csch}(\beta l)\sin(\beta l)} & \frac{\cos(\beta l) - \coth(\beta l)\sin(\beta l)}{1 - \operatorname{csch}(\beta l)\sin(\beta l)} \end{pmatrix}. \tag{17}$$

Mapping of the flexural periodic waveguide with pinned supports onto the SSH model

We map the periodic flexural waveguide in Fig. 1a to the discrete lattice shown in Fig. 1b, following an analytical approach similar to that proposed in[48,74] for acoustic waveguides. Notice that the nodes x_n^{A} of the discrete system correspond to the change of material from phase B to phase A, going in the positive x-direction, whereas the nodes x_n^{B} correspond to the change of material from phase A to phase B.

First, we assume continuity of rotations and bending moments at the nodes:

$$[[\Theta]] = 0, \ [[M]] = [[-EI\Theta']] = 0, \tag{18}$$

expressed in terms of jumps [[]]. Next, we calculate the rotations at each node, using the transfer matrix $\boldsymbol{T}$ in (16). Specifically, considering the junctions at the right and left of x_n^{A}, we can write:

$$\begin{gathered} \Theta(x_n^{\mathrm{B}}) = \boldsymbol{T}_{11}^{\mathrm{A}}\Theta(x_n^{\mathrm{A}}) + \boldsymbol{T}_{12}^{\mathrm{A}}M(x_n^{\mathrm{A}}), \\ \Theta(x_{n-1}^{\mathrm{B}}) = \left(\boldsymbol{T}_{11}^{\mathrm{B}}\right)^{-1}\Theta(x_n^{\mathrm{A}}) + \left(\boldsymbol{T}_{12}^{\mathrm{B}}\right)^{-1}M(x_n^{\mathrm{A}}) = \boldsymbol{T}_{11}^{\mathrm{B}}\Theta(x_n^{\mathrm{A}}) - \boldsymbol{T}_{12}^{\mathrm{B}}M(x_n^{\mathrm{A}}), \end{gathered} \tag{19}$$

where the subscript of $\boldsymbol{T}$ indicates the entry of the transfer matrix, while the superscript denotes the phase (A or B). Upon eliminating the bending moment $M(x_n^{\mathrm{A}})$ from both Eqs. (19), we obtain an equation expressed in terms of rotations. We repeat the procedure for the two nodes around x_n^{B}. In addition, since the system is spatially periodic, we impose Bloch conditions, i.e. $\Theta(x_{n+1}^{\mathrm{A}}) = \Theta(x_n^{\mathrm{A}})\mathrm{e}^{\mathrm{i}kL}$ and $\Theta(x_{n-1}^{\mathrm{B}}) = \Theta(x_n^{\mathrm{B}})\mathrm{e}^{-\mathrm{i}kL}$, where k is the wavenumber. Furthermore, we assume that $\beta_{\mathrm{A}}l_{\mathrm{A}} = \beta_{\mathrm{B}}l_{\mathrm{B}} = \beta l$, which is a necessary condition to establish a mapping between the periodic flexural beam and the discrete SSH model. We recall that β_i is the frequency-like parameter given by $\beta_i = \sqrt[4]{\rho_i A_i\omega^2/(E_i I_i)}$ (i = A, B).

Accordingly, we obtain a system of two equations in the two unknowns $\Theta(x_n^{\mathrm{A}}) \equiv \mathcal{A}$ and $\Theta(x_n^{\mathrm{B}}) \equiv \mathcal{B}$, given by

$$\begin{gathered} \left\{\left(E_{\mathrm{A}}I_{\mathrm{A}}\beta_{\mathrm{A}} + E_{\mathrm{B}}I_{\mathrm{B}}\beta_{\mathrm{B}}\right)\left[\cos(\beta l) - \coth(\beta l)\sin(\beta l)\right]\right\}\mathcal{A} \\ +\left\{\left(E_{\mathrm{A}}I_{\mathrm{A}}\beta_{\mathrm{A}} + E_{\mathrm{B}}I_{\mathrm{B}}\beta_{\mathrm{B}}\mathrm{e}^{-\mathrm{i}kL}\right)\left[\operatorname{csch}(\beta l)\sin(\beta l) - 1\right]\right\}\mathcal{B} = 0, \\ \left\{\left(E_{\mathrm{A}}I_{\mathrm{A}}\beta_{\mathrm{A}} + E_{\mathrm{B}}I_{\mathrm{B}}\beta_{\mathrm{B}}\mathrm{e}^{\mathrm{i}kL}\right)\left[\operatorname{csch}(\beta l)\sin(\beta l) - 1\right]\right\}\mathcal{A} \\ +\left\{\left(E_{\mathrm{A}}I_{\mathrm{A}}\beta_{\mathrm{A}} + E_{\mathrm{B}}I_{\mathrm{B}}\beta_{\mathrm{B}}\right)\left[\cos(\beta l) - \coth(\beta l)\sin(\beta l)\right]\right\}\mathcal{B} = 0\,. \end{gathered} \tag{20}$$

This system leads to the eigenvalue problem (1).

Bending moment mapping for the beam system with pinned supports

Following the mapping of the flexural periodic waveguide with pinned supports onto the SSH model using the rotation as the mapping variable, we now demonstrate that an equivalent mapping can be achieved by employing the bending moment as the mapping variable, in line with the approach reported in[47,50]. As in the case of the rotation-based mapping, our starting point is the continuity of rotations and bending moments at the nodes, expressed by Eq. (18).

Next, we employ the transfer matrix $\boldsymbol{T}$ in (16) to calculate the bending moment at each node:

$$\begin{gathered} M(x_n^{\mathrm{B}}) = \boldsymbol{T}_{21}^{\mathrm{A}}\Theta(x_n^{\mathrm{A}}) + \boldsymbol{T}_{22}^{\mathrm{A}}M(x_n^{\mathrm{A}}), \\ M(x_{n-1}^{\mathrm{B}}) = \left(\boldsymbol{T}_{21}^{\mathrm{B}}\right)^{-1}\Theta(x_n^{\mathrm{A}}) + \left(\boldsymbol{T}_{22}^{\mathrm{B}}\right)^{-1}M(x_n^{\mathrm{A}}) = -\boldsymbol{T}_{21}^{\mathrm{B}}\Theta(x_n^{\mathrm{A}}) + \boldsymbol{T}_{22}^{\mathrm{B}}M(x_n^{\mathrm{A}}). \end{gathered} \tag{21}$$

As for the rotation mapping, we eliminate the rotation $\Theta(x_n^{\mathrm{A}})$ from both Eqs. (21), to obtain an equation expressed in terms of bending moments. We repeat the procedure for the two nodes around x_n^{B}. In addition, we impose Bloch conditions, i.e. $M(x_{n+1}^{\mathrm{A}}) = M(x_n^{\mathrm{A}})\mathrm{e}^{\mathrm{i}kL}$ and $M(x_{n-1}^{\mathrm{B}}) = M(x_n^{\mathrm{B}})\mathrm{e}^{-\mathrm{i}kL}$. We recall that we have assumed $\beta_{\mathrm{A}}l_{\mathrm{A}} = \beta_{\mathrm{B}}l_{\mathrm{B}} = \beta l$.

After some algebra, we obtain the following eigenvalue problem for the two unknown bending moments $M(x_n^{\mathrm{A}}) \equiv \mathcal{A}_M$ and $M(x_n^{\mathrm{B}}) \equiv \mathcal{B}_M$:

$$\begin{pmatrix} 0 & \mathscr{u}_M + \mathscr{w}_M\,\mathrm{e}^{-\mathrm{i}kL} \\ \mathscr{u}_M + \mathscr{w}_M\,\mathrm{e}^{\mathrm{i}kL} & 0 \end{pmatrix}\begin{pmatrix} \mathcal{A}_M \\ \mathcal{B}_M \end{pmatrix} = E(\beta l)\begin{pmatrix} \mathcal{A}_M \\ \mathcal{B}_M \end{pmatrix}, \tag{22}$$

where the energy and couplings are

$$\begin{gathered} E(\beta l) = \frac{\cos(\beta l) - \coth(\beta l)\sin(\beta l)}{1 - \operatorname{csch}(\beta l)\sin(\beta l)}, \\ \mathscr{u}_M = \frac{Q_{\mathrm{B}}}{Q_{\mathrm{A}} + Q_{\mathrm{B}}},\ \mathscr{w}_M = \frac{Q_{\mathrm{A}}}{Q_{\mathrm{A}} + Q_{\mathrm{B}}}, \end{gathered} \tag{23}$$

with Q_i defined in (3). Notice that the effective energy $E(\beta l)$ is the same as for the rotation mapping, which indicates that the mappings are isospectral.

By comparing the set of couplings of the bending moment mapping $(\mathscr{u}_M,\mathscr{w}_M)$ to the set of the rotation mapping $(\mathscr{u},\mathscr{w})$, we have: $\mathscr{u} \to \mathscr{w}_M$ and $\mathscr{w} \to \mathscr{u}_M$. Consequently, for the same bulk, the two different mappings have inverse topological phases.

Derivation of the transfer matrix for an Euler-Bernoulli beam element with sliding supports

Here, we study an Euler-Bernoulli beam constrained by sliders at its ends (see Fig. 16), which prevent rotations and allow transverse displacements.

Using the expression (10) for the transverse displacement amplitude, we obtain that the rotation amplitude is given by

$$\Theta(x) = V'(x) = \beta\left[-A_1\sin(\beta x) + A_2\cos(\beta x) + A_3\sinh(\beta x) + A_4\cosh(\beta x)\right], \tag{24}$$

where β is the frequency-like parameter defined in (11).

By setting $V'(x=0) = 0$ and $V'(x=l) = 0$, we can express the unknown coefficients A_3 and A_4 in terms of A_1 and A_2. Then, we derive:

$$\boldsymbol{\Upsilon}(x) = \begin{pmatrix} V(x) \\ T(x) \end{pmatrix} = \boldsymbol{Z}(x)\boldsymbol{A}, \tag{25}$$

where $\boldsymbol{\Upsilon}(x)$ represents the generalized vector including the amplitudes of the kinematic (the transverse displacement $V(x)$) and static (the shear force $T(x) = -EIV'''(x)$) variables, $\boldsymbol{A} = \left(A_1\ A_2\right)^{\mathrm{T}}$ stands for the vector of unknowns, and

$$\begin{aligned} &\boldsymbol{Z}(x) \\ &= \begin{pmatrix} \cos(\beta x) + \mathcal{G}(\beta l)\cosh(\beta x) & \sin(\beta x) - \sinh(\beta x) - \mathcal{F}(\beta l)\cosh(\beta x) \\ -EI\beta^3\left[\sin(\beta x) + \mathcal{G}(\beta l)\sinh(\beta x)\right] & EI\beta^3\left[\cos(\beta x) + \cosh(\beta x) + \mathcal{F}(\beta l)\sinh(\beta x)\right] \end{pmatrix} \end{aligned} \tag{26}$$

where the functions $\mathcal{F}(\beta l)$ and $\mathcal{G}(\beta l)$ are given in (14).

Following the same procedure as that for the beam with hinged ends, we find that the generalized eigenvector $\boldsymbol{\Upsilon}(x_{\mathrm{R}}) = \boldsymbol{Z}(x_{\mathrm{R}})\boldsymbol{Z}^{-1}(x_{\mathrm{L}})\boldsymbol{\Upsilon}(x_{\mathrm{L}})$, where $\overline{\boldsymbol{T}} = \boldsymbol{Z}(x_{\mathrm{R}})\boldsymbol{Z}^{-1}(x_{\mathrm{L}})$ is the *transfer matrix* for a beam element with sliding supports at the ends, given by

$$\overline{\boldsymbol{T}} = \begin{pmatrix} \frac{\cos(\beta l)+\coth(\beta l)\sin(\beta l)}{1+\operatorname{csch}(\beta l)\sin(\beta l)} & \frac{\cos(\beta l)\coth(\beta l)+\operatorname{csch}(\beta l)}{-EI\beta^3\left[1+\operatorname{csch}(\beta l)\sin(\beta l)\right]} \\ \frac{-2EI\beta^3\sin(\beta l)}{1+\operatorname{csch}(\beta l)\sin(\beta l)} & \frac{\cos(\beta l)+\coth(\beta l)\sin(\beta l)}{1+\operatorname{csch}(\beta l)\sin(\beta l)} \end{pmatrix}, \tag{27}$$

and characterized by $\det(\overline{\boldsymbol{T}}) = 1$.

Mapping of the flexural periodic waveguide with sliding supports onto the SSH model

The mapping procedure from the flexural waveguide represented in Fig. 9a to the discrete SSH model sketched in Fig. 9b is based on the same steps described for the pin-supported structure, including the assumption $\beta_A l_A = \beta_B l_B = \beta l$.

In this case, the junction conditions are expressed as $[[V]] = 0$ and $[[T]] = [[-EIV''']] = 0$.

Using the transfer matrix in (27), we retrieve the following system of equations:

$$\begin{gathered} \left\{-\left(E_A I_A \beta_A^3 + E_B I_B \beta_B^3\right)\left[\cos(\beta l) + \coth(\beta l)\sin(\beta l)\right]\right\}\mathcal{C} \\ +\left\{\left(E_A I_A \beta_A^3 + E_B I_B \beta_B^3 \mathrm{e}^{-\mathrm{i}kL}\right)\left[1 + \operatorname{csch}(\beta l)\sin(\beta l)\right]\right\}\mathcal{D} = 0, \\ \left\{\left(E_A I_A \beta_A^3 + E_B I_B \beta_B^3 \mathrm{e}^{\mathrm{i}kL}\right)\left[1 + \operatorname{csch}(\beta l)\sin(\beta l)\right]\right\}\mathcal{C} \\ +\left\{-\left(E_A I_A \beta_A^3 + E_B I_B \beta_B^3\right)\left[\cos(\beta l) + \coth(\beta l)\sin(\beta l)\right]\right\}\mathcal{D} = 0, \end{gathered} \tag{28}$$

where $\mathcal{C} \equiv V(x_n^A)$ and $\mathcal{D} \equiv V(x_n^B)$. The system above yields the eigenvalue problem (7).

Shear force mapping for the beam system with sliding supports

As demonstrated for the flexural periodic waveguide with pinned supports, there are two equivalent mappings onto the SSH model, using the rotation or bending moment as the mapping variables. This is also the case for the flexural periodic waveguide with sliding supports, where now the mapping variables are the displacement and the shear force.

Following the displacement mapping, we consider the continuity of displacement and shear force in the nodes of the system, namely $[[V]] = 0$ and $[[T]] = [[-EIV''']] = 0$.

Next, we employ the transfer matrix $\overline{\boldsymbol{T}}$ in (27) to calculate the shear force at each node, and by eliminating the displacement $V(x_n^A)$ we obtain an equation expressed in terms of shear forces. We repeat the procedure for the two nodes around x_n^B. In addition, we impose Bloch conditions, i.e., $T(x_{n+1}^A) = T(x_n^A)\mathrm{e}^{\mathrm{i}kL}$ and $T(x_{n-1}^B) = T(x_n^B)\mathrm{e}^{-\mathrm{i}kL}$. Again, we point out that we have assumed $\beta_A l_A = \beta_B l_B = \beta l$.

After some algebra, we obtain the following eigenvalue problem for the two unknown shear forces $T(x_n^A) \equiv \mathcal{C}_T$ and $T(x_n^B) \equiv \mathcal{D}_T$:

$$\begin{pmatrix} 0 & \overline{\varpi}_T + \overline{\varpi}_T\,\mathrm{e}^{-\mathrm{i}kL} \\ \overline{\varpi}_T + \overline{\varpi}_T\,\mathrm{e}^{\mathrm{i}kL} & 0 \end{pmatrix}\begin{pmatrix} \mathcal{C}_T \\ \mathcal{D}_T \end{pmatrix} = \overline{E}(\beta l)\begin{pmatrix} \mathcal{C}_T \\ \mathcal{D}_T \end{pmatrix}, \tag{29}$$

where the energy and couplings are

$$\begin{gathered} \overline{E}(\beta l) = \frac{\cos(\beta l)+\coth(\beta l)\sin(\beta l)}{1+\operatorname{csch}(\beta l)\sin(\beta l)}, \\ \overline{\varpi}_T = \frac{P_B}{P_A+P_B},\ \overline{\varpi}_T = \frac{P_A}{P_A+P_B}, \end{gathered} \tag{30}$$

with P_i defined in (9), while the effective energy $\overline{E}(\beta l)$ is the same as for the displacement mapping, which indicates that the mappings are isospectral.

By comparing the set of couplings of the shear force mapping $(\overline{\varpi}_T, \overline{\varpi}_T)$ to the set of the displacement mapping $(\overline{\varpi}, \overline{\varpi})$, we have: $\overline{\varpi} \to \overline{\varpi}_T$ and $\overline{\varpi} \to \overline{\varpi}_T$. Consequently, for the same bulk, the two different mappings have inverse topological phases, as for the case of the flexural waveguide with pinned supports.

Data availability

The main data supporting the findings of this study are available within this paper. The codes used to analyze the data and generate the plots for this manuscript are available from the corresponding author upon request.

Received: 17 January 2026; Accepted: 9 June 2026;
Published online: 06 July 2026

References

1. Ozawa, T. et al. Topological photonics. *Rev. Mod. Phys.* **91**, 015006 (2019).
2. Wu, L.-H. & Hu, X. Scheme for achieving a topological photonic crystal by using dielectric material. *Phys. Rev. Lett.* **114**, 223901 (2015).
3. Zhang, X., Zangeneh-Nejad, F., Chen, Z.-G., Lu, M.-H. & Christensen, J. A second wave of topological phenomena in photonics and acoustics. *Nature* **618**, 687–697 (2023).
4. Süsstrunk, R. & Huber, S. D. Classification of topological phonons in linear mechanical metamaterials. *Proc. Natl. Acad. Sci. USA.* **113**, E4767–E4775 (2016).
5. Mousavi, S. H., Khanikaev, A. B. & Wang, Z. Topologically protected elastic waves in phononic metamaterials. *Nat. Commun.* **6**, 8682 (2015).
6. Ma, G., Xiao, M. & Chan, C. T. Topological phases in acoustic and mechanical systems. *Nat. Rev. Phys.* **1**, 281–294 (2019).
7. Xue, H., Yang, Y. & Zhang, B. Topological acoustics. *Nat. Rev. Mater.* **7**, 974–990 (2022).
8. Zhang, X., Xiao, M., Cheng, Y., Lu, M. & Christensen, J. Topological sound. *Commun. Phys.* **1**, 97 (2018).
9. Kane, C. L. & Mele, E. J. Quantum spin hall effect in graphene. *Phys. Rev. Lett.* **95**, 226801 (2005).
10. Hasan, M. Z. & Kane, C. L. Colloquium: Topological insulators. *Rev. Mod. Phys.* **82**, 3045–3067 (2010).
11. Brendel, C., Peano, V., Painter, O. & Marquardt, F. Snowflake phononic topological insulator at the nanoscale. *Phys. Rev. B* **97**, 020102R (2018).
12. Khanikaev, A. B. et al. Photonic topological insulators. *Nat. Mater.* **12**, 233–239 (2013).
13. Lu, L., Joannopoulos, J. D. & Soljačić, M. Topological photonics. *Nat. Photon.* **8**, 821–829 (2014).
14. Wang, P., Lu, L. & Bertoldi, K. Topological phononic crystals with one-way elastic edge waves. *Phys. Rev. Lett.* **115**, 104302 (2015).
15. Huber, S. D. Topological mechanics. *Nat. Phys.* **12**, 621–623 (2016).
16. Pal, R. K. & Ruzzene, M. Edge waves in plates with resonators: an elastic analogue of the quantum valley hall effect. *N. J. Phys.* **19**, 025001 (2017).
17. Chen, B., Upadhyaya, N. & Vitelli, V. Nonlinear conduction via solitons in a topological mechanical insulator. *Proc. Natl. Acad. Sci. USA.* **111**, 13004–13009 (2014).
18. Craster, R. V. & Davies, B. Asymptotic characterization of localized defect modes: Su−Schrieffer–Heeger and related models. *Multiscale Model. Sim.* **21**, 827–848 (2023).
19. Wang, A., Zhou, Y. & Chen, C. Q. Topological mechanics beyond wave dynamics. *J. Mech. Phys. Solids* **173**, 105197 (2023).
20. Wu, B. et al. Wave manipulation in intelligent metamaterials: Recent progress and prospects. *Adv. Funct. Mater.* **34**, 2316745 (2024).
21. Morvaridi, M. et al. Tunable topologically protected waveguiding in auxetic nonlinear metamaterials. *Phys. Rev. Appl.* **21**, 034024 (2024).
22. Garau, M., Nieves, M. J., Carta, G. & Brun, M. Transient response of a gyro-elastic structured medium: Unidirectional waveforms and cloaking. *Int. J. Eng. Sci.* **143**, 115–141 (2019).
23. Carta, G., Colquitt, D., Movchan, A., Movchan, N. & Jones, I. One-way interfacial waves in a flexural plate with chiral double resonators. *Philos. Trans. R. Soc. A* **378**, 20190350 (2020).

24. Carta, G., Nieves, M. J., Brun, M. & Pagneux, V. Edge resonance in discrete elastic waveguides and its convergence to isotropic continuous media. *Int. J. Eng. Sci.* **215**, 104307 (2025).
25. Chen, Z., Morini, L. & Gei, M. Design of interface modes in canonical phononic waveguides. *J. Mech. Phys. Solids* **204**, 106291 (2025).
26. Su, W. P., Schrieffer, J. R. & Heeger, A. J. Solitons in polyacetylene. *Phys. Rev. Lett.* **42**, 1698–1701 (1979).
27. Asbóth, J. K., Oroszlány, L. & Pályi, A. A short course on topological insulators, vol. 919 of *Lecture Notes in Physics* (Springer, 2016).
28. Delplace, P., Ullmo, D. & Montambaux, G. Zak phase and the existence of edge states in graphene. *Phys. Rev. B* **84**, 195452 (2011).
29. Ryu, S., Schnyder, A. P., Furusaki, A. & Ludwig, A. W. Topological insulators and superconductors: tenfold way and dimensional hierarchy. *N. J. Phys.* **12**, 065010 (2010).
30. Asbóth, J. K. Symmetries, topological phases, and bound states in the one-dimensional quantum walk. *Phys. Rev. B* **86**, 195414 (2012).
31. Franke, K. J. & von Oppen, F. Designer topology in graphene nanoribbons. *Nature* **560**, 175 (2018).
32. Gröning, O. et al. Engineering of robust topological quantum phases in graphene nanoribbons. *Nature* **560**, 209–213 (2018).
33. Rizzo, D. J. et al. Topological band engineering of graphene nanoribbons. *Nature* **560**, 204–208 (2018).
34. Padić, K., Hegde, S. S., DeGottardi, W. & Vishveshwara, S. Topological phases, edge modes, and the hofstadter butterfly in coupled Su–Schrieffer–Heeger systems. *Phys. Rev. B* **98**, 024205 (2018).
35. Liu, F. & Wakabayashi, K. Novel topological phase with a zero Berry curvature. *Phys. Rev. Lett.* **118**, 076803 (2017).
36. Kim, M. & Rho, J. Topological edge and corner states in a two-dimensional photonic Su–Schrieffer–Heeger lattice. *Nanophotonics* **9**, 3227–3234 (2020).
37. Zheng, L., Achilleos, V., Richoux, O., Theocharis, G. & Pagneux, V. Observation of edge waves in a two-dimensional Su–Schrieffer–Heeger acoustic network. *Phys. Rev. Appl.* **12**, 034014 (2019).
38. Xiao, Y.-X., Ma, G., Zhang, Z. & Chan, C. T. Topological subspace-induced bound state in the continuum. *Phys. Rev. Lett.* **118**, 166803 (2017).
39. Liao, D. et al. Observations of tamm modes in acoustic topological insulators. *Appl. Phys. Lett.* **120**, 211701 (2022).
40. Guo, H. & Chen, S. Kaleidoscope of symmetry-protected topological phases in one-dimensional periodically modulated lattices. *Phys. Rev. B* **91**, 041402 (2015).
41. Huda, M. N., Kezilebieke, S., Ojanen, T., Drost, R. & Liljeroth, P. Tuneable topological domain wall states in engineered atomic chains. *npj Quantum Mater.* **5**, 17 (2020).
42. Zhang, S.-L. & Zhou, Q. Two-leg Su–Schrieffer–Heeger chain with glide reflection symmetry. *Phys. Rev. A* **95**, 061601 (2017).
43. Jangjan, M. & Hosseini, M. V. Topological properties of subsystem-symmetry-protected edge states in an extended quasi-one-dimensional dimerized lattice. *Phys. Rev. B* **106**, 205111 (2022).
44. Guo, Q.-H., Zhang, Y., Wan, X. & Zheng, L. Observation of chiral edge state pairs in an acoustic trimer waveguide. *Appl. Phys. Lett.* **126**, 133102 (2025).
45. Guo, Q., Zhang, Y., Wan, X. & Zheng, L. Isospectral reduction of the trimer Su–Schrieffer–Heeger lattice and its bulk-edge correspondence. *Phys. Rev. Appl.* **23**, L031001 (2025).
46. Yin, J. et al. Band transition and topological interface modes in 1d elastic phononic crystals. *Sci. Rep.* **8**, 6806 (2018).
47. Allein, F. et al. Strain topological metamaterials and revealing hidden topology in higher-order coordinates. *Nat. Commun.* **14**, 6633 (2023).
48. Coutant, A. et al. Acoustic Su–Schrieffer–Heeger lattice: Direct mapping of acoustic waveguides to the Su–Schrieffer–Heeger model. *Phys. Rev. B* **103**, 224309 (2021).
49. Xiao, M. et al. Geometric phase and band inversion in periodic acoustic systems. *Nat. Phys.* **11**, 240–244 (2015).
50. Ioannou Sougleridis, I. et al. Existence and characterization of edge states in an acoustic trimer Su–Schrieffer–Heeger model. *Phys. Rev. B* **110**, 174311 (2024).
51. Chaplain, G. J. et al. Tunable topological edge modes in Su–Schrieffer–Heeger arrays. *Appl. Phys. Lett.* **122**, 221703 (2023).
52. Chaplain, G. J., De Ponti, J. M., Aguzzi, G., Colombi, A. & Craster, R. V. Topological rainbow trapping for elastic energy harvesting in graded Su–Schrieffer–Heeger systems. *Phys. Rev. Appl.* **14**, 054035 (2020).
53. Chen, Z., Zhi, G., Wang, G., Guo, T. & Chang, S. Topological elastic metamaterials for wave manipulation: a comprehensive review. *J. Phys.: Condens. Matter* **37**, 453001 (2025).
54. Dal Poggetto, V. F., Pal, R. K., Pugno, N. M. & Miniaci, M. Topological bound modes in phononic lattices with nonlocal interactions. *Int. J. Mech. Sci.* **281**, 109503 (2024).
55. Miniaci, M., Pal, R. K., Morvan, B. & Ruzzene, M. Experimental observation of topologically protected helical edge modes in patterned elastic plates. *Phys. Rev. X* **8**, 031074 (2018).
56. Zhang, Y., Zheng, L. & Christensen, J. Defect-immune sound radiation in a topologically nontrivial hyperbolic metamaterial. *Phys. Rev. Lett.* **134**, 156602 (2025).
57. Zheng, L. & Christensen, J. Dirac hierarchy in acoustic topological insulators. *Phys. Rev. Lett.* **127**, 156401 (2021).
58. Li, T. et al. Acoustic möbius insulators from projective symmetry. *Phys. Rev. Lett.* **128**, 116803 (2022).
59. Kane, C. L. & Lubensky, T. C. Topological boundary modes in isostatic lattices. *Nat. Phys.* **10**, 39–45 (2014).
60. Tang, Z., Ma, F., Li, F., Yao, Y. & Zhou, D. Fully polarized topological isostatic metamaterials in three dimensions. *Phys. Rev. Lett.* **133**, 106101 (2024).
61. Meng, Y. et al. Designing topological interface states in phononic crystals based on the full phase diagrams. *N. J. Phys.* **20**, 073032 (2018).
62. Cajić, M., Karličić, D., Christensen, J. & Adhikari, S. Tunable topological interface states in one-dimensional inerter-based locally resonant lattices with damping. *J. Sound Vib.* **542**, 117326 (2023).
63. Cajić, M., Christensen, J. & Adhikari, S. Tuning of topological interface modes in an elastic beam array system with inerters. *Int. J. Mech. Sci.* **205**, 106573 (2021).
64. Zhou, D. Topological boundary modes in nonlinear dynamics with chiral symmetry. *N. J. Phys.* **26**, 073009 (2024).
65. Carta, G. & Brun, M. Bloch–floquet waves in flexural systems with continuous and discrete elements. *Mech. Mater.* **87**, 11–26 (2015).
66. Chen, Z., Gei, M. & Morini, L. Flexural wave propagation in canonical quasicrystalline-generated waveguides. *Int. J. Solids Struct.* **305**, 113050 (2024).
67. Carta, G., Salis, A. & Meloni, D. Modelling bridges and pipelines as periodic Timoshenko-Ehrenfest beams. *Int. J. Solids Struct.* **332**, 113945 (2026).
68. Zak, J. Berry's phase for energy bands in solids. *Phys. Rev. Lett.* **62**, 2747 (1989).
69. Kawarabayashi, T. & Hatsugai, Y. Bulk-edge correspondence with generalized chiral symmetry. *Phys. Rev. B* **103**, 205306 (2021).
70. Anastasiadis, A., Styliaris, G., Chaunsali, R., Theocharis, G. & Diakonos, F. K. Bulk-edge correspondence in the trimer Su–Schrieffer–Heeger model. *Phys. Rev. B* **106**, 085109 (2022).
71. Ma, T.-X., Fan, Q.-S., Zhang, C. & Wang, Y.-S. Flexural wave energy harvesting by the topological interface state of a phononic crystal beam. *Extrem. Mech. Lett.* **50**, 101578 (2022).

72. Xiao, M., Zhang, Z. Q. & Chan, C. T. Surface impedance and bulk band geometric phases in one-dimensional systems. *Phys. Rev. X* **4**, 021017 (2014).
73. Graff, K. F. Wave Motion in Elastic Solids (Dover, New York, 1991).
74. Coutant, A., Achilleos, V., Richoux, O., Theocharis, G. & Pagneux, V. Subwavelength Su–Schrieffer–Heeger topological modes in acoustic waveguides. *J. Acoust. Soc. Am.* **151**, 3626–3632 (2022).

Acknowledgements

The authors are grateful to Georgios Theocharis and Vincent Pagneux for the helpful discussion. G.C., L.M., and M.B. acknowledge the support of the Fondazione di Sardegna through the project FdS 2023 "Smart Materials and Morphing Systems for efficient energy harvesting based on fluid-structure interactions" (F23C25000280007).

Author contributions

G.C.: conceptualization, formal analysis, interpretation of the data, draft. I.I.S.: conceptualization, formal analysis, interpretation of the data, draft. L.M.: conceptualization, interpretation of the data, text review. M.B.: conceptualization, interpretation of the data, text review.

Competing interests

The authors declare no competing interests.

Additional information

Correspondence and requests for materials should be addressed to Michele Brun.

Reprints and permissions information is available at http://www.nature.com/reprints

Publisher's note Springer Nature remains neutral with regard to jurisdictional claims in published maps and institutional affiliations.